Solar RRL
www.solar-rrl.com

Design and Characterization of a 53.5% Efficient Gallium Indium Phosphide-Based Optical Photovoltaic Converter under 637 nm Laser Irradiation at 10 W cm^{-2}

Pablo Sanmartín, Eduardo F. Fernández,* Antonio García-Loureiro, Jesús Montes-Romero, Aitana Cano, Pablo Martín, Ignacio Rey-Stolle, Iván García, and Florencia Almonacid*

High-power optical transmission (HPOT) technology has emerged as a promising alternative among far-field wireless power transmission approaches, enabling the transfer of kilowatts of power over kilometer-scale distances. Its exceptional adaptability allows operation in challenging scenarios where traditional electrical wiring is impractical or unfeasible, thereby opening up a vast array of potential applications previously considered utopian. An important pending assignment in enhancing the performance of laser-based HPOT systems is achieving efficient photovoltaic conversion of high power densities (≥10 W cm^{-2}). In this sense, there is a pressing need for the advancement of optical photovoltaic converters (OPCs) capable of enduring intense monochromatic irradiances. This work presents the design optimization, manufacturing, and characterization processes of a gallium indium phosphide (GaInP)-based OPC under varying 637 nm laser power at room temperature. In addition, methods to evaluate the impact of temperature on performance are provided. The findings reveal a maximum efficiency of 53.5% at 10 W cm^{-2}, surpassing literature results for GaInP converters by over 9%$_{abs}$ at those light intensities. Remarkably, this device withstands unmatched irradiances within GaInP OPCs up to 60 W cm^{-2}, maintaining 42.3% efficiency. This study aims to push forward the development of wide-bandgap power converters with recordbreaking efficiencies paving the way for new applications.

1. Introduction

High-power optical transmission (HPOT) has recently been gaining traction as one of the most promising wireless power transmission (WPT) technologies.[1] It utilizes a monochromatic light, typically emitted by a laser, to power remote electronic devices through a photovoltaic (PV) cell, commonly known as optical photovoltaic converter (OPC) or laser power converter (LPC). HPOT systems overcome limitations inherent to traditional wiring, providing solutions in situations where the use of electrical cables is not recommended, unsafe, or directly impossible.[2]

Already situated in a billion-dollar market,[3] and capable of transferring hundreds of watts over kilometric distances,[4] this technology has the potential to revolutionize the energy transmission sector. The prospective applications are endless, including powering robots,[5] small aircrafts,[6,7] remote sensors,[8] satellites,[9,10] or to transfer both power and data to militarized unmanned equipment with high-level security. Furthermore, HPOT applications are not only restricted to the atmosphere domain. For instance, efforts are being made to deploy a virtual grid in the outer space to power remote habitats and landing facilities that could replenish exploration mission mobile units in situations in which solar energy harvesting is impractical, such as in dark sides of planets or during solar eclipses or even to uninterruptedly power the Earth from space-based solar power stations.[11–14] In addition, the implementation of HPOT technology in submarine environments is also under study.[15,16] Despite its extraordinary potential, HPOT is yet to advance beyond the initial development stage, requiring considerable efforts to enhance the efficiency, currently around 20%, and the power flux transfer capacity, limited to ≈100 W cm^{-2}.[1] The immense

P. Sanmartín, E. F. Fernández, J. Montes-Romero, F. Almonacid
Advances in Photovoltaic Technology (AdPVTech)
CEACTEMA
University of Jaén
23071 Jaén, Spain
E-mail: pandujar@ujaen.es; eduardo.fernandez@ujaen.es

The ORCID identification number(s) for the author(s) of this article can be found under https://doi.org/10.1002/solr.202400278.

DOI: 10.1002/solr.202400278

A. García-Loureiro
Centro Singular de Investigación en Tecnoloxías de Información (CiTiUS)
Departament of Electronics and Computer Science
Universidade de Santiago de Compostela
15782 Santiago de Compostela, Spain

A. Cano, P. Martín, I. Rey-Stolle, I. García
Instituto de Energía Solar
ETSI of Telecommunications
Universidad Politécnica de Madrid
28040 Madrid, Spain

number of prospective applications endorse the need for further efforts to fully exploit this technology.

One of the most critical components on the overall efficiency of the HPOT systems is the OPC. Nowadays, state-of-the-art converters are based on III–V compounds. Among these, gallium arsenide (GaAs) stands out, renowned for being an extensively studied and well-established semiconductor material in PV[17,18] and for holding the efficiency record at room temperature, $68.9 \pm 2.8\%$ at $11.4\ \mathrm{W\,cm^{-2}}$.[19] However, theoretical studies suggest that alternative materials might be more suitable for monochromatic PV conversion[20,21] and can be used indistinctly in different environments.[22]

A major concern about HPOT is the severe efficiency reduction observed in the OPCs under high-input power density conditions. This decrease is mainly attributed to the series resistance losses associated with the elevated currents generated at such intense illuminations.[17] To face this challenge, wider bandgap semiconductors are proposed as suitable candidates.[20,22,23] This type of materials produces less current compared to lower energy gap (E_g) semiconductors due to the nature of the incident photons, thus diminishing the associated series resistance losses.[23] Added to this, an increase in bandgap energy results in a reduction of intrinsic losses, particularly those related to entropy.[20] In this sense, the use of higher-energy-gap materials as gallium indium phosphide (GaInP, $E_g = 1.85\ \mathrm{eV}$) should moderate the aforementioned losses compared to narrower-bandgap materials, such as GaAs ($E_g = 1.42\ \mathrm{eV}$). Furthermore, the manufacturing of GaInP PV devices has reached an advanced stage, being extensively used in concentrator PV (CPV) and space PV as the top cell in multijunction solar cells,[24] alongside the production of several OPCs.[25–28]

In this work, we present the design process, manufacturing, and performance characterization of a GaInP OPC under varying power densities at room temperature (298 K), where the device fabrication and experimental setup are described in detail. In addition, a comprehensive experimental analysis is conducted, with particular emphasis on the temperature-related challenges inherent to the characterization of these devices. We propose methods to quantify their potential impact and to delimit the associated uncertainty, which represent a relevant yet underexplored topic in the literature. The results show a maximum efficiency of $53.5 \pm 0.2\%$ under 637 nm monochromatic laser light at an input power density of $10\ \mathrm{W\,cm^{-2}}$, surpassing by more than $9\%_{abs}$ the literature results of GaInP-based OPCs at this power density level. Additionally, it represents an overall improvement of nearly $7\%_{abs}$ compared to peak efficiencies achieved at lower power densities.[27,28] Furthermore, the reported OPC achieves an efficiency as high as $42.3 \pm 0.2\%$ at $60\ \mathrm{W\,cm^{-2}}$ light intensity. This is intended to be a first step toward the development of recordbreaking efficient wide-bandgap OPCs suitable for HPOT applications at high light input powers.

2. Experimental Section

In this section, the design, fabrication, and characterization processes of a GaInP-based OPC are described.

2.1. Design and Optimization

In order to streamline the typically extensive development time of gradually implementing improvements and to avoid the high manufacturing cost associated, we opted to utilize a technology computer-aided design (TCAD) modeling tool to design and optimize the device structure. We used Silvaco Atlas Device Simulator,[29] a reliable physics-based TCAD software capable of accurately replicating the performance of semiconductor devices, such as CPV solar cells and OPC.[30,31] During the simulation process, an analytical low-field mobility model was employed, and all concentration-dependent recombination mechanisms (Shockley–Read–Hall, radiative, and Auger), along with surface and interface recombinations, were considered to reproduce and optimize the behavior of our GaInP-based OPC device. Also, the temperature was set constant at 298 K as a first step in the design of the OPC. Further work will investigate other temperature operations to achieve higher efficiencies depending on the expected operation regime.

The modeling phase started with an exhaustive compilation of information related to the semiconductor materials properties projected to be employed, namely GaInP (p–n junction), AlInP (window layer), and AlGaInP (back surface field [BSF] layer). Key parameters including charge carrier mobilities and lifetimes,[32–35] energy gaps,[32,34,35] optical indexes,[36] permittivities,[35,37,38] and effective masses[35,37,38] were thoroughly addressed for each material. Afterward, we performed an optimization with the objective of maximizing efficiency under an incident power density of $100\ \mathrm{W\,cm^{-2}}$. During this process, the light source wavelength, doping concentrations, and layer thicknesses were systematically varied within feasible ranges, limited by technical constraints established in collaboration with our manufacturer partner, the Instituto de Energía Solar – Universidad Politécnica de Madrid (IES-UPM).

2.2. Device Fabrication

The device fabrication was carried out at facilities in the Instituto de Energía Solar – Universidad Politécnica de Madrid. The semiconductor structure was deposited by metal-organic vapor-phase epitaxy (MOVPE) using an AIX200/4 horizontal reactor from AIXTRON. The precursor molecules used were TMGa, TMAl, TMIn, DMZn, DTBSi, DETe, AsH_3, and PH_3 for the corresponding elements. The work pressure was 100 mbar and the setpoint temperature was kept at 675 °C along the growth. The structure was deposited on Zn-doped GaAs substrates with a [100] orientation and a miscut of 2° toward the (111)B plane. The GaInP absorber layers were deposited at a growth rate of 3.4 µm/hr and a V/III ratio of 100. The thicknesses of the layers deposited, measured using an in situ EpiRAS 2000 monitoring tool with an uncertainty of ±5%, are indicated in **Figure 1**.

The semiconductor structure was processed into solar cell devices with a $1.40 \times 1.55\ \mathrm{mm^2}$ die area and a typical comb front grid design using a 150 µm-wide busbar and 18 fingers 3 µm wide, see Figure 1 (right). It is worth mentioning that this grid distribution deviates from the previously obtained theoretical optimizations. Instead, we implemented a configuration intended for CPV applications corresponding to the available

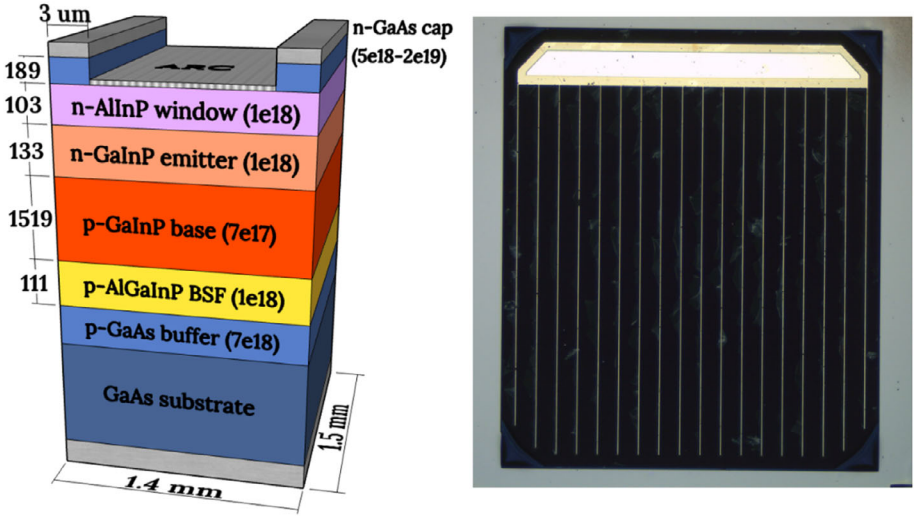

Figure 1. Left: Scheme of the OPC structure (not to scale). ARC stands for antireflection coating, and BSF for back surface field. The doping concentrations are specified by the numbers in parenthesis in cm^{-3}, with an associated uncertainty of ±20%. Unless specified, layer thicknesses are expressed in nm. Right: Picture of the receiving surface of the device.

photolithography masks, which will impact the performance of the device, as will be further discussed later. This front grid design was defined using standard photolithography techniques and e-beam evaporation to form a metal stack based on the Pd/Ge/Ti/Pd/Al system,[39] with a 1000 nm-thick Al layer. The back contact was deposited using thermal evaporation and was based on an Au/AuZn/Au stack with a total thickness of 600 nm. MgF_2/ZnS (100 nm/50 nm) double-layer antireflection coating (ARC) was deposited using e-beam evaporation, with a thickness configuration designed to minimize the reflectance at 640 nm. The power converter devices were isolated using a mesa chemical etch step and saw dicing. Finally, the resulting chips were encapsulated by soldering them to an insulated metal substrate (IMS) combining copper and ceramic layers to achieve insulation with the back side and good thermal management. The front grid bus was connected to a pad on the IMS using aluminum wire bonding. For the sake of clarity and summarization, the processing scheme is shown in **Figure 2**.

2.3. Device Characterization

The characterization process was carried out at Centro de Estudios Avanzados en Ciencias de la Tierra, Energía y Medio Ambiente (CEACTEMA) facilities of the University of Jaen. External quantum efficiency (EQE) and spectral response (SR) were measured using a grating monochromator setup (Bentham, PVE300). A 0.74 mm-wide exit slit was selected, which allowed to perform 1 nm step sweeps across wavelengths from 300 to 700 nm. The procedure was repeated three times. It is worth mentioning that the minimum light spot area achieved closely corresponded to the device area ($\approx 1.4 \times 1.2\ mm^2$), which may have derived in slightly undesired light losses and, therefore, a minor underestimation in EQE/SR values.

The *I*–*V* measurement setup (**Figure 3**) was designed to enable measurements at variable monochromatic irradiances. The system equipment included a 10 W continuous-wave fiber-coupled laser (CNI laser, MDL-XF-640, $\lambda = 637$ nm), an attached automatic shutter (Thorlabs, SHB025, 3 ms rise/fall time), a thermal power sensor (Ophir, 50(150)A-BB-26), a charge-coupled device (CCD) camera (Ophir, SP920s), a source meter unit (Keysight B2902B), and a temperature-controlled chuck (QInstruments, ColdPlate).

After the light travels through the optical fiber, a beam homogenizing collimator was employed to obtain a 2.65 mm-side flat-top squared pattern light spot, as illustrated in **Figure 4**. The OPC was placed at the center of the light spot, as represented by the black dashed rectangle in Figure 4 (left). In this delimited region, the light exhibited nonuniformity of 2.3%. Also, the beam presented well-collimated normal incidence, as indicated by the vertical 3D representation in Figure 4 (right). Finally, the effective illuminated surface was determined by considering only points where light intensity exceeded 75% of the maximum registered intensity, resulting in a total of 5.38 mm^2.

The *I*–*V* measurement methodology was conducted in the following manner. First, the input power density was adjusted to the desired value. Due to laser instability at lower irradiances, the light source power was doubled checked using the thermal power sensor both before and after each measurement. After setting the laser power, the *I*–*V* curves were recorded through 160–170 ms sweeps, maintaining the temperature-controlled chuck fixed at 298 K. This procedure was iterated, gradually increasing input power values from 1.6 up to 60 $W\,cm^{-2}$. Analogously to the EQE/SR measurements, three sets of measurements were carried out. The data displayed in the plots throughout the article represent the mean values of the obtained results, with error bars indicating the standard deviation, as the systematic error associated with the measurement tools is negligible in comparison with the previous ones.

Given the strong temperature dependence of the open-circuit voltage and the rapid temperature rise experienced, especially at

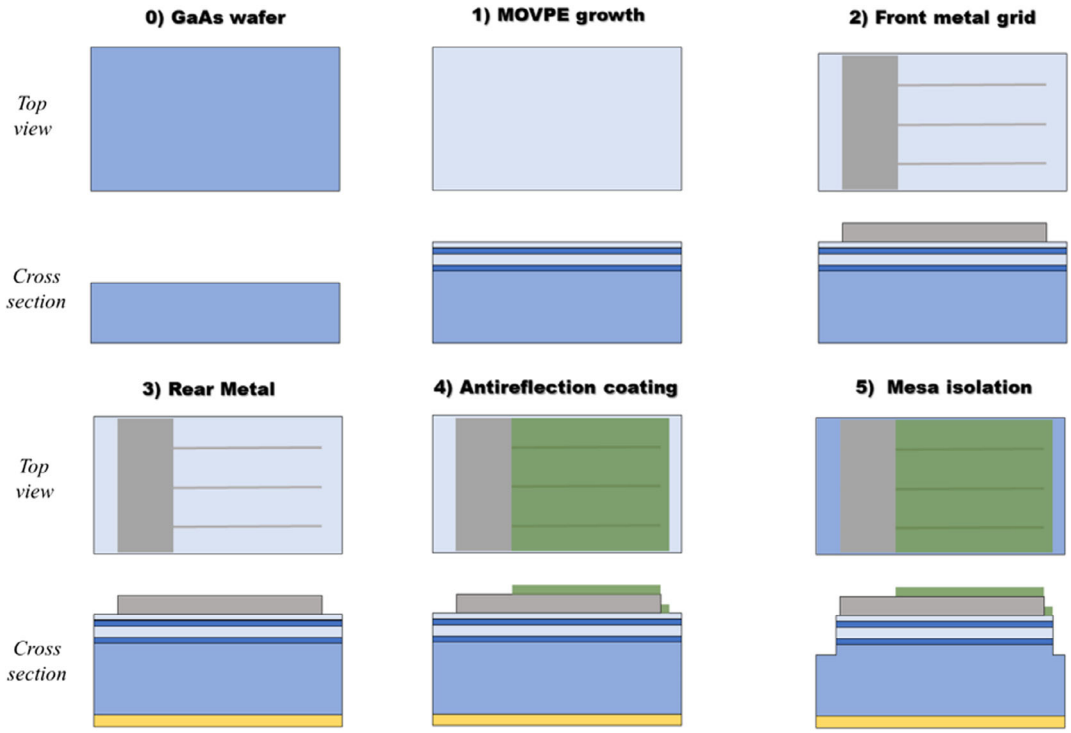

Figure 2. Diagram of the fabrication steps to realize the OPC of this work [40]. 0) Initial GaAs substrate. 1) Semiconductor structure deposition by MOVPE. 2) Front-side metal grid processing. 3) Rear-side contact metallization. 4) Deposition of ARC on the front side. 5) Isolation of the power converter device, with a posterior encapsulation to an IMS.

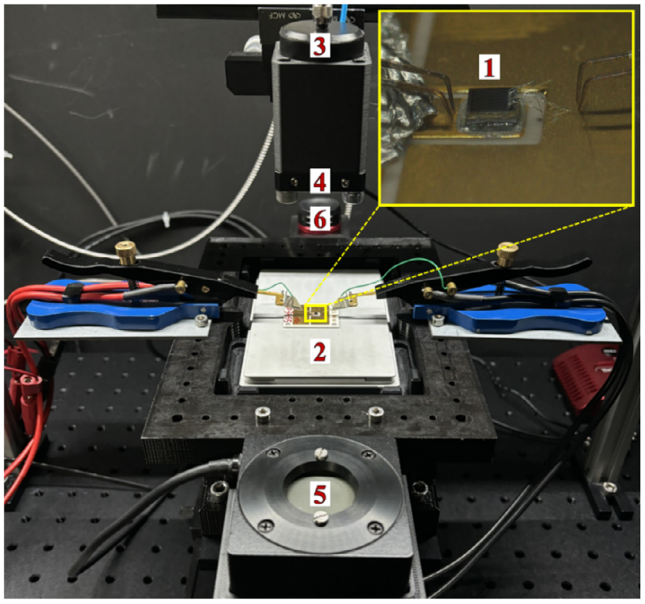

Figure 3. Picture of the laser measurement setup. The OPC (#1, closed-up view of the inset) is fixed on a temperature-controlled chuck (#2) that can be adjusted in X–Y–Z directions. The OPC sample is contacted by Kelvin probes. The homogenizing collimator (#3) and the automatic shutter (#4) are mounted in a self-designed mobile holding piece oriented perpendicularly to the cell. The thermal power sensor (#5) and the CCD camera (#6) are aligned on the same axis, positioned at the front and the back of the image, respectively. A digital microscope (not shown) is used to ensure the OPC is properly illuminated and centered with respect to the beam.

intense illuminations (>10 W cm^{-2}), we opted to perform backward *I–V* measurements, that is, from open-circuit voltage to short-circuit current direction ($V_{OC} \rightarrow I_{SC}$), as a strategy to mitigate the adverse temperature effects. This method allowed the extraction of V_{OC} within the first 15 ms of laser illumination. In addition, in order to evaluate more precisely this dependence, we also conducted V_{OC}-only measurements as a function of temperature at different irradiances using a thermocouple sensor placed as close to the device as possible, see inset in Figure 3 for visual illustration.

3. Results and Discussion

The EQE and SR results are presented in **Figure 5**. The maximum EQE is achieved at 538 nm, registering a value of $89.62 \pm 0.03\%$. Beyond this point, there is a slight decrease up to 670 nm, where a steep fall is observed, approximately coinciding with the cutoff wavelength expected for the $Ga_{0.51}In_{0.49}P$ energy gap: 1.85 eV. At the operational wavelength (637 nm, refer to Section 2), the EQE is equal to $85.21 \pm 0.02\%$. As for the SR, an experimental peak value of $439.7 \pm 0.1 \times 10^{-3}$ AW^{-1} is reached at 628 nm, whereas SR of $437.8 \pm 0.1 \times 10^{-3}$ AW^{-1} is obtained in this device at 637 nm. The operational SR is remarkably close to its maximum value, suggesting effective device design and appropriate laser wavelength selection, thereby achieving optimum performance.

Next, we will examine the characteristic parameters extracted from the measured *I–V* curves. Starting with the short-circuit

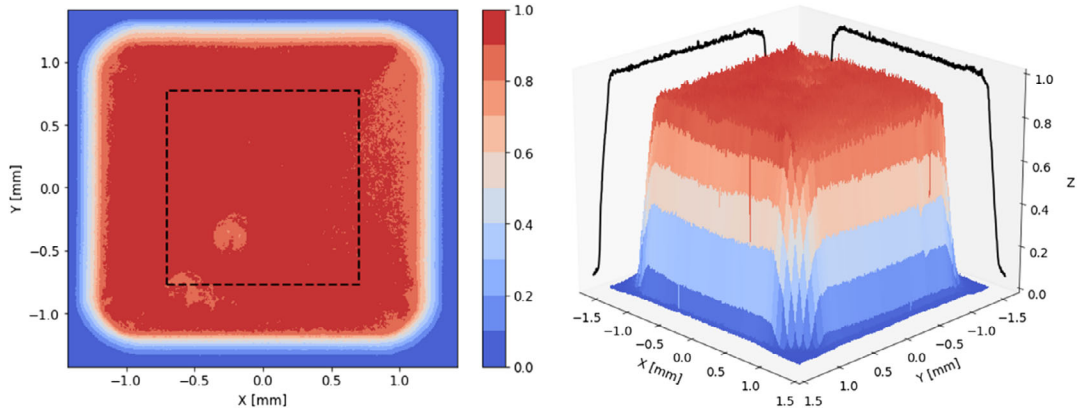

Figure 4. 2D (left) and 3D (right) representations of the laser beam. The black dashed rectangle in the left plot indicates the position of the OPC. The color map (left) and the Z-axis (right) are normalized to the maximum power.

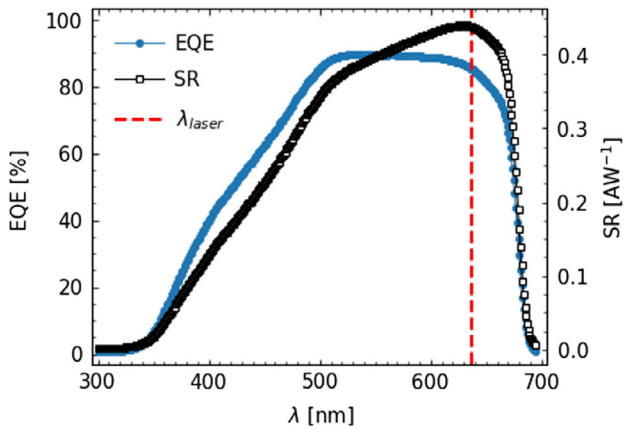

Figure 5. Measured EQE and SR as a function of wavelength. The red dashed line corresponds to the operational laser wavelength ($\lambda = 637$ nm). Note: error bars not included for reasons of visual clarity.

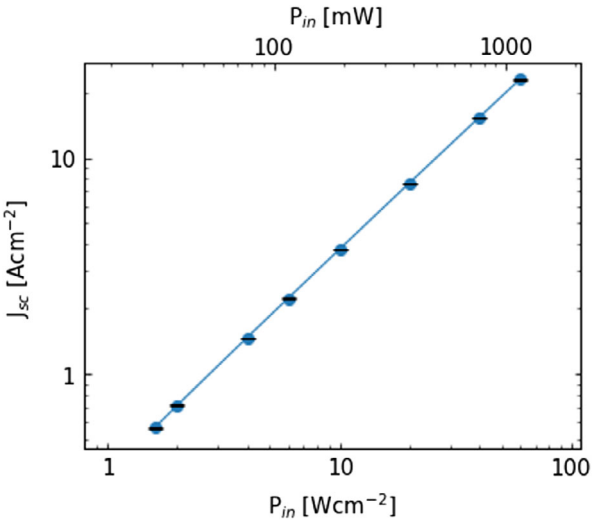

Figure 6. Short-circuit current density versus input power density.

current density (J_{SC}), it demonstrates a linear behavior with respect to the input power density, ranging from 0.561 ± 0.005 A cm^{-2} at 1.6 W cm^{-2} to 23.2 ± 0.1 A cm^{-2} at 60 W cm^{-2}, as depicted in **Figure 6**, confirming the anticipated direct correlation.

As for the V_{OC}, particularly in the medium power density range (1–10 W cm^{-2}), its value increases proportionally to the logarithm of irradiance, ranging from 1.4548 ± 0.0008 V at 1.6 W cm^{-2} to 1.527 ± 0.002 V at 10 W cm^{-2}, as illustrated in **Figure 7**. Fitting the medium power measured V_{OC}–I_{SC} data to a one-diode model yields an ideality factor (n) of 1.5. Considering that ideality factor values of 1 and 2 are associated with charge carrier recombination in neutral and depletion (p–n junction) regions,[41] respectively, an ideality factor falling midway implies that the recombination mechanism originating from traps in the space–charge region of the cell is of a similar order of magnitude to the one in the quasineutral region. Furthermore, we also measured the dark I–V curve, obtaining a dark saturation current density (J_0) of 2.9×10^{-18} A cm^{-2}, and a corresponding n of 1.44, which corroborates the previous results and is in accordance with previous studies.[42] The ideality factor is significantly higher when comparing with the state-of-the-art GaAs OPCs, 1.08,[19] which manifest that GaInP devices experience considerable nonradiative minority carrier recombination, particularly in the base and in the space–charge region.[32]

However, when illumination reaches higher power densities (≥10 W cm^{-2}), the V_{OC} experiences a significative decrease from the expected values (represented by the dashed orange line in Figure 7), outputting 1.5697 ± 0.0005 V at 60 W cm^{-2} and implying a voltage drop of 9, 21, and 31 mV for 20, 40, and 60 W cm^{-2}, respectively. We believe that this deviation in the high-power region can be explained by the combination of two phenomena. On one hand, the increase in current, resulting from the intensified input power, might saturate the energy traps in the space–charge region. This, in turn, would neutralize the associated recombination centers, and the ideality factor shifts toward unity, ultimately derived in the reduction of V_{OC}.[43] This effect can be

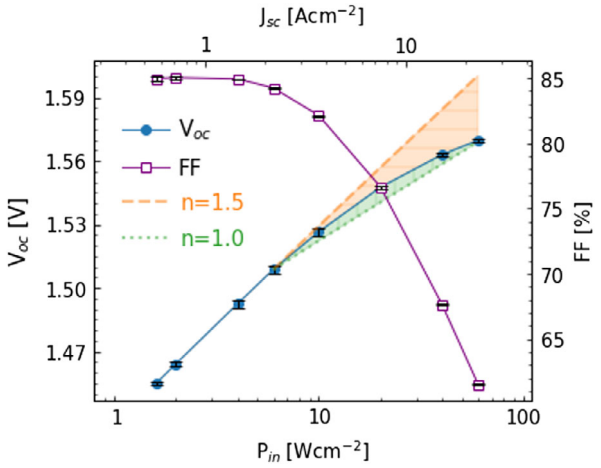

Figure 7. V_{OC} and FF as a function of input power density. The orange dashed line and the green dotted line represent hypothetical V_{OC} projections assuming ideality factors of 1.5 and 1.0, respectively.

observed in Figure 7, where V_{OC} progressively approaches the projected $n = 1$ values represented by the dotted green line.

On the other hand, temperature emerges as arguably the most crucial and common factor affecting V_{OC}.[43,44,45] First, in order to assess its potential impact on the overall performance of the device, we conducted a separate analysis of the behavior of V_{OC} with respect to temperature at different high power densities. As presented in **Figure 8** (left), the V_{OC} exhibits an inverse linear dependence on temperature. This correlation enables the extraction of the temperature coefficients (TC) and relative temperature coefficients (TC_{rel}) for the designated power densities (Figure 8 (right)). The absolute values of the coefficients consistently decrease with rising input powers, ranging from $-1.81\,m\,VK^{-1}$ ($-0.118\%K^{-1}$) at $10\,W\,cm^{-2}$ to $-1.47\,m\,VK^{-1}$ ($-0.093\,\%K^{-1}$) at $100\,W\,cm^{-2}$. The obtained TC_{rel} are comparable to those found in other III–V semiconductors widely used in OPCs and CPV solar cells reported in literature, such as GaAs.[46,47]

Finally, assuming the voltage drop from the $n = 1.5$ projection is solely due to temperature effects, the device temperature can be estimated. For the sake of simplicity, we considered the temperature measured by the sensor the effective PV converter temperature, neglecting heat conduction losses. The results indicate maximum variations of 5.4, 12.8 and 19.4 K for 20, 40, and $60\,W\,cm^{-2}$, respectively. In the eventuality of such scenario, the abrupt temperature rise would present a concerning challenge within the context of high-power applications. Addressing this issue would require at least the implementation of effective cooling mechanisms to regulate excessive heating. On a side note, it is important to bear in mind that, at high power densities, both aforementioned phenomena, namely, the approximation of the ideality factor to the radiative limit ($n = 1$) and the increase in temperature, occur simultaneously, making it unfeasible to assess their individual effects independently.

The measured fill factor (FF) reaches its maximum of $85.0 \pm 0.1\%$ at $2\,W\,cm^{-2}$, and high values (>80%) are maintained through the medium-power-density region (Figure 7). However, when the irradiance enters the high-power region ($>10\,W\,cm^{-2}$), the FF suffers a rapid decrease, dropping to $61.5 \pm 0.1\%$ at $60\,W\,cm^{-2}$. Precisely, the decline of the FF aligns with the degradation of the V_{OC}, as shown in Figure 7.

The efficiency of the OPC across various input power densities is presented in **Figure 9**, which compares simulation results with experimental measurements. The results obtained from the simulation clearly confirm the trend of the experimental results and closely match the peak efficiency value. The discrepancy in the results could be explained due to the simulation considering a device with more idealized models and that in the manufacturing stage there are always factors that have not been adequately accounted for in simulation modeling. Also, the parameters were optimized and thoroughly studied for high-power levels, but not exhaustively investigated for lower-power ranges, where materials might exhibit different behavior, possibly accounting for the trend deviation.

The measured data (blue circles) exhibits an increasing trend, starting from $49.1 \pm 0.5\%$ at $1.6\,W\,cm^{-2}$ up to its peak of $53.5 \pm 0.2\%$ at $10\,W\,cm^{-2}$. Beyond that threshold, the performance of the OPC experiences a significant decline, reducing

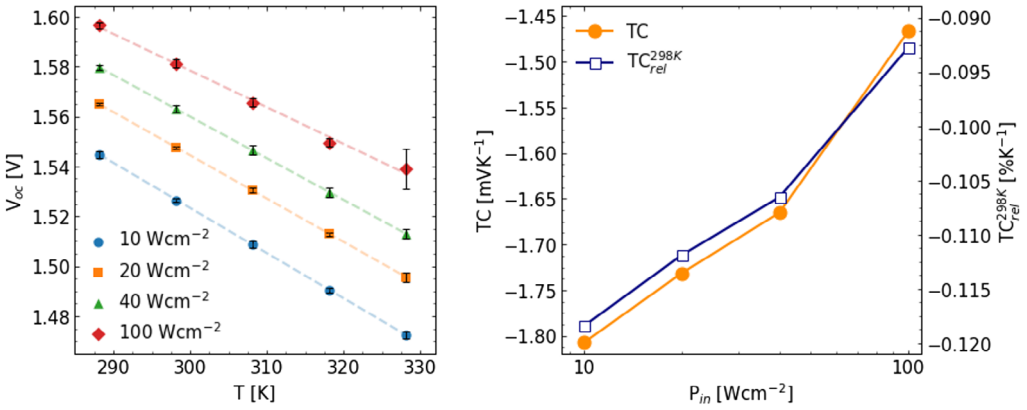

Figure 8. V_{OC} as a function of temperature for various high power densities (left) and TC and TC_{rel} versus irradiance (right). Relative TCs are normalized to V_{OC} at 298 at 298 at 298 K. Temperature effects are observed to be more significant at high irradiances; hence, only power densities greater than or equal to $10\,W\,cm^{-2}$ were considered. Coefficients for $60\,W\,cm^{-2}$ were interpolated from the available data.

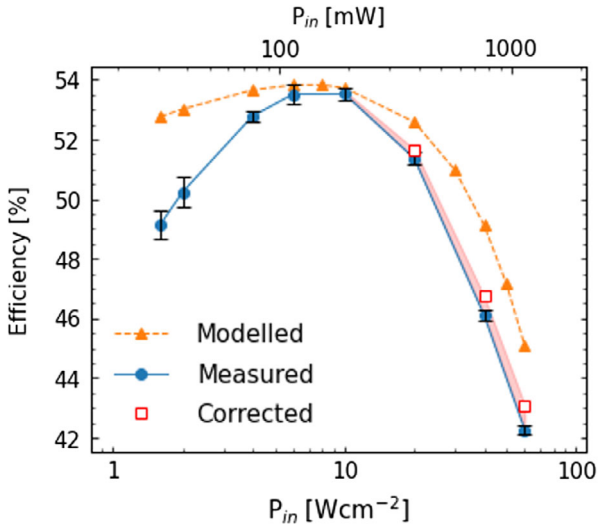

Figure 9. Simulated, measured, and corrected efficiencies versus input irradiance.

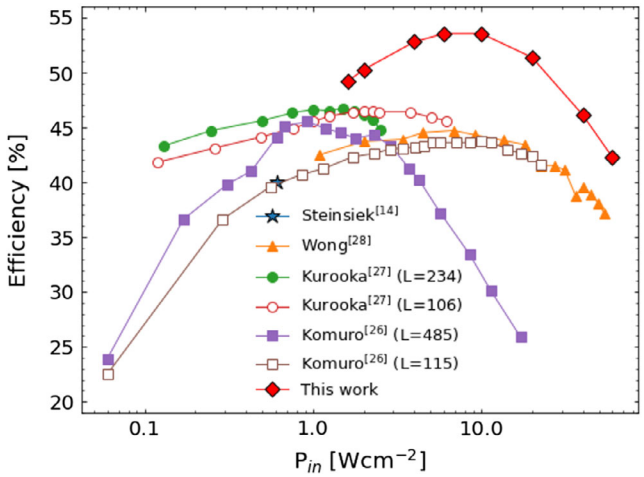

Figure 10. Efficiency versus incident power density of state-of-the-art GaInP-based OPCs. In the legend, *L* distinguishes the OPCs from the reference, indicating the finger spacing in micrometer.

the efficiency by more than 10%$_{abs}$ (42.3 ± 0.2%) when a power density of 60 W cm^{-2} is reached. This severe decrease may be attributed to the substantial series resistance losses (R_S) at high-power densities, as they escalate quadratically with current ($R_S I^2$), and to the high lateral resistance compared to other state-of-the-art materials, such as GaAs.[26] This behavior is commonly found in OPC-related literature.[17,21,45,48] Some strategies to try to mitigate these negative effects are to further optimize the contact grid configuration[27,49] or to fabricate OPCs based on wide-bandgap semiconductor materials (≥2.5 eV), as this would reduce the generated current or with smaller characteristic series resistance.[22,23]

Furthermore, in an effort to bypass the impact of temperature on the overall performance of the device at high-input power densities, we calculated the hypothetical efficiency at 298 K. For this purpose, the measured output power was corrected assuming that the TCs of I_{SC} and FF are negligible compared to V_{OC}'s TC, that is, the efficiency variations caused by temperature are solely dependent on changes in the open-circuit voltage. The corrected efficiency (red squares) at 298 K (Figure 9) improves the measured performances in 0.3 (51.7%), 0.6 (46.7%), and 0.8%$_{abs}$ (43.1%) at 20, 40, and 60 W cm^{-2}, respectively.

To contextualize the results, **Figure 10** shows a comparison of the most efficient GaInP-based OPCs available in literature. Currently, our device stands out as the best in terms of efficiency, outperforming the second ones by ≈9.2%$_{abs}$ at 10 W cm^{-2}[28] and 2.4%$_{abs}$ at around 1.6 W cm^{-2},[27] resulting in an overall improvement of 6.8%$_{abs}$ when comparing peak efficiencies. Notably, it is also the power converter that has been tested at the highest power density, achieving 42.3 ± 0.2% efficiency at 60 W cm^{-2}, in contrast to the 37.2% obtained by the closest GaInP OPC in literature, even at a lower irradiance of 53.5 W cm^{-2}.[28] Moreover, it demonstrates effective operation at medium power densities, making it particularly suitable for HPOT applications.

Nonetheless, it is evident that GaInP devices suffer significant losses at high power densities or even before in some cases, which highlights the urge to address this issue. For instance, the results presented by Kurooka et al.[27] (circles) and Komuro et al.[26] (squares) using two different finger spacings and thicknesses confirm that implementing previously discussed loss mitigation strategies helps maintain high efficiencies at elevated power densities, despite causing a slight reduction of the maximum values. Indeed, the utilization of optimized denser grids (empty symbols) leads to a delayed and more gradual degradation in performance. Applying this enhancement to the device proposed in this study could potentially yield an efficiency of over 40% at 100 W cm^{-2}.

Finally, the optimal loads (R_m) of various OPC examples available in literature are presented in **Figure 11**. It is important to note that, in practice, an optimal load larger than ≈1 Ω is crucial for reducing high output currents and mitigating the consequential external parasitic resistive losses, such as wiring, as well as

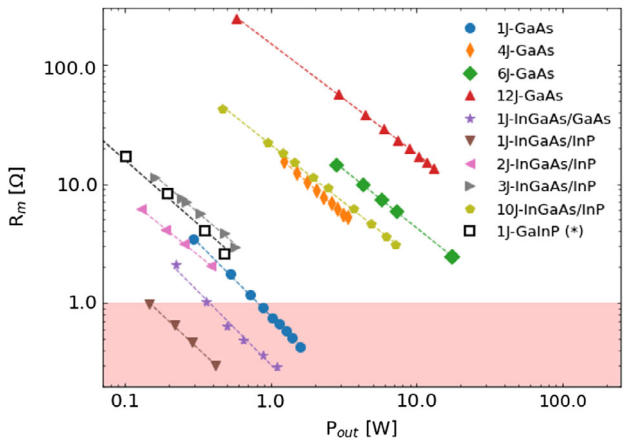

Figure 11. Optimal load versus output power of different types of OPCs available in literature.[51] The red area indicates a high-current and low-voltage region associated with practically unfeasible values of R_m. The numbers in the legend correspond to the number of junctions forming the converters. The results from this study are denoted by (*).

other resistance losses within the device related to charge carrier extraction, including gridline and sheet conduction resistances.[18] Therefore, it is advisable to achieve the highest possible output voltage to prevent the collapse of R_m to unfeasibly small values. In this sense, our single-junction device (1 J-GaInP), apart from exhibiting practically viable results ($R_m > 1\,\Omega$) throughout all tested intensities, demonstrates enhanced optimal load compared to other single- and even double-junction (2 J) OPCs, closely approaching the values of triple-junction (3 J) devices. This achievement is remarkable, considering multijunction cells display higher voltage and lower currents than single-junction devices of the same materials, resulting in higher R_m, as shown in Figure 11.

Furthermore, GaInP-based OPC exhibiting higher optimal loads than GaAs, InGaAs/GaAs, or InGaAs/InP can be attributed to the fact that wider-bandgap semiconductors generate less photocurrent density at the same input power, thereby increasing the optimal load, since it is inversely proportional to the current.

GaInP OPCs demonstrate promising potential in efficiently converting medium power densities. Nonetheless, additional enhancements are necessary to raise the maximum efficiency and to minimize the performance degradation observed at intense irradiances. A thorough investigation of the V_{OC} decrease should be conducted, along with the exploration of methods to mitigate the significant nonradiative recombination, whether through improved manufacturing techniques or alternative advanced design strategies. For instance, implementing a back metal reflector would reduce the device thickness improving the optical confine, ultimately resulting in an enhanced V_{OC}.[50] However, this could imply substantial modifications in the semiconductor structure and fabrication process, which could affect the thermal management, among other potential difficulties that would need to be carefully considered. Also, an optimization of the grid configuration should be studied in future work to try reduce the R_s losses and improve the FF at extreme light intensities. Moreover, considerable attention should also be directed toward addressing temperature-related issues, as their impact on performance must be adequately minimized for HPOT to become a viable solution. Additionally, it is advisable to explore novel materials with higher-energy gaps and reduced characteristic series resistance to further develop the technology.

4. Conclusion

This work demonstrates the viability of GaInP-based OPCs for prospective HPOT applications. To carry out this study, a GaInP PV converter was first designed and optimized for high power densities using Silvaco TCAD software. After fabrication of the device by the IES-UPM, it was experimentally characterized at the CEACTEMA laboratory of University of Jaén employing 637 nm uniform laser illumination. The *I–V* curves were recorded for input power densities within 1.6–60 W cm^{-2} and at a controlled room temperature of 298 K.

Results show an $85.21 \pm 0.02\%$ EQE and a $437.8 \pm 0.1 \times 10^{-3}$ AW^{-1} SR at the operational wavelength. Regarding the parameters extracted from the *I–V* measurements, the short-circuit current density (J_{SC}) increases linearly with irradiance. As for the open-circuit voltage (V_{OC}), it increases proportionally to the logarithm of the irradiance up to medium power densities ($\approx$10 W cm^{-2}), where a decrease from expected values is observed. This deviation could be attributed to a combined effect of the reduction of the ideality factor (n) and the abrupt rise in temperature at high illumination levels. Additionally, to determine the impact of temperature, a separate analysis of V_{OC} temperature dependence was conducted, obtaining a maximum variation of 19.4 K at 60 W cm^{-2} when considering that the voltage drop was solely caused by temperature. Regarding the FF, it exhibits a peak of $85.0 \pm 0.1\%$ at 2 W cm^{-2}, followed by a pronounced decrease, coinciding with V_{OC} behavior. Finally, the device demonstrates an increasing efficiency up to 10 W cm^{-2}, where a maximum of $53.5 \pm 0.2\%$ is obtained. Beyond that point, the efficiency experiences a marked decline due to the strong impact of series resistance. Nevertheless, our device outperforms state-of-the-art GaInP-based OPCs by more than $9\%_{abs}$ at 10 W cm^{-2} and was able to withstand the highest input power density tested to date. Moreover, the characteristic optimal load presents practically feasible values.

Despite the positive results obtained, further improvements need to be accomplished to surpass the milestones achieved by GaAs-based OPCs. Future work should study in depth the impact of temperature, beam uniformity, and alternative grid patterns on the performance. Furthermore, the investigation of the manufacturing feasibility of groundbreaking higher-energy gap materials that also exhibit lower inherent series resistance can lead to unprecedented efficiencies.

Acknowledgements

This work was partially funded by the project "UltraMicroCPV" (MICINN-Agencia Estatal de Investigación: PID2019-106497RB-I00/ AEI /10.13039/501100011033) and by the project NACe-CPV/TE (Junta de Andalucía, PAIDI 2020: P18-RT-1595). E.F.F. thanks the Spanish Ministry of Science, Innovation and Universities because of the Ramón y Cajal 2017 fellowships (RYC-2017-2191). The authors thank Luis Cifuentes, Jesús Bautista, and Manuel Abuin for technical assistance during device processing. This work was partially supported by the Grant PID2021-123530OB-I00 funded by Ministerio de Ciencia e Innovación (MCIN/AEI/10.13039/501 100 011 033), the epitaxy runs reported in this article were carried out in a metal-organic vapor-phase epitaxy reactor retrofitted with project RENOAIX200 (grant no. EQC2019-005701-P) funded also by Spanish MCIN/AEI (AEI/10.13039/501 100 011 033) and FEDER "Una manera de hacer Europa". Part of the equipment used in this research for solar cell manufacturing was acquired through project LABCELL30 [(grant no. EQC2021-006851-P) with funding from the Spanish Ministerio de Ciencia e Innovación/Agencia Estatal de Investigación (MCIN/AEI 10.13039/501 100 011 033) and the European Union "Next Generation EU"/PRTR", European Regional Development Fund (ERDF) "A way to make Europe" and by the Universidad Politécnica de Madrid through "Ayudas para la cofinanciación de infraestructuras de I + D + I (Programa Propio)."

Conflict of Interest

The authors declare no conflict of interest.

Data Availability Statement

The data that support the findings of this study are available from the corresponding author upon reasonable request.

Keywords

GaInP, III–V materials, photovoltaics, power converters, wireless power transmissions

Received: April 9, 2024
Revised: May 30, 2024
Published online: June 14, 2024

[1] K. Jin, W. Zhou, *IEEE Trans. Power Electron.* **2019**, *34*, 3842.
[2] S. Y. R. Hui, W. Zhong, C. K. Lee, *IEEE Trans. Power Electron.* **2014**, *29*, 4500.
[3] X. Lu, P. Wang, D. Niyato, D. I. Kim, Z. Han, *IEEE Commun. Surveys Tutorials* **2016**, *18*, 1413.
[4] H. Yigit, A. R. Boynuegri, *IEEE Access.* IEEE, Piscataway, NJ, **2023**.
[5] N. Kawashima, K. Takeda, H. Matsuoka, Y. Fujii, M. Yamamoto, *ISARC Proceedings.* **2005**.
[6] T. Blackwell, *AIP Conf. Proc.* **2005**, *766*, 73.
[7] K. Takeda, N. Kawashima, K. Yabe, *Chin. Opt. Lett.* **2007**, *5*, S109.
[8] K. Worms, C. Klamouris, F. Wegh, L. Meder, D. Volkmer, S. P. Philipps, S. K. Reichmuth, H. Helmers, A. Kunadt, J. Vourvoulakis, A. W. Bett, C. Koos, W. Freude, J. Leuthold, W. Stork, *Wind Energy* **2017**, *20*, 345.
[9] D. Shi, L. Zhang, H. Ma, Z. Wang, Y. Wang, Z. Cui, *IEEE Wireless Power Transfer Conf.*, IEEE, Piscataway, NJ, **2016**.
[10] M. Sanders, J. S. Kang *IEEE Aerospace Conf. Proc.*, IEEE, Piscataway, NJ, **2020**
[11] Y. Zheng, G. Zhang, Z. Huan, Y. Zhang, G. Yuan, Q. Li, G. Ding, Z. Lv, W. Ni, Y. Shao, X. Liu, J. Zu, *Space Solar Power Wireless Trans.* **2024**.
[12] S. Abdullah, P. J. S. Mulles, R. E. Amaya, *IEEE Int. Conf. Wireless for Space and Extreme Environments (WiSEE)*, IEEE, Piscataway, NJ, **2022**, p. 49.
[13] D. E. Becker, R. Chiang, C. C. Keys, A. W. Lyjak, J. A. Nees, M. D. Starch, C. Phipps, K. Komurasaki, J. Sinko, *Photovoltaic-Concentrator Based Power Beaming For Space Elevator Application*, **2010**, pp. 271–281.
[14] F. Steinsiek, K. H. Weber, W. P. Foth, H. J. Foth, Schafer, C., *8th ESA Workshop on Advanced Space Technologies for Robotics and Automation*, **2004**, pp. 1–10.
[15] S. A. H. Mohsan, M. A. Khan, A. Mazinani, M. H. Alsharif, H.-S. Cho, *J. Mar. Sci. Eng.* **2022**, *10*, 1282.
[16] S.-M. Kim, J. Choi, H. Jung, *Chin. Opt. Lett.* **2018**, *16*, 80101.
[17] C. Algora, I. García, M. Delgado, R. Peña, C. Vázquez, M. Hinojosa, I. Rey-Stolle, *Joule* **2022**, *6*, 340.
[18] S. Fafard, D. P. Masson, *J. Appl. Phys.* **2021**, *130*, 160901.
[19] H. Helmers, E. Lopez, O. Höhn, D. Lackner, J. Schön, M. Schauerte, M. Schachtner, F. Dimroth, A. W. Bett, *Phys. Status Solidi – RRL* **2021**, *15*.
[20] M. Lin, W. E. I. Sha, W. Zhong, D. Xu, *Appl. Phys. Lett.* **2021**, *118*.
[21] E. Oliva, F. Dimroth, A. W. Bett, *Prog. Photovoltaics* **2008**, *16*, 289.
[22] P. Sanmartín, F. Almonacid, M. A. Ceballos, A. García-Loureiro, E. F. Fernández, *Solar Energy Mater. Solar Cells* **2024**, *266*, 112662.
[23] E. F. Fernández, A. García-Loureiro, N. Seoane, F. Almonacid, *Solar Energy Mater. Solar Cells* **2022**, 235.
[24] A. Baiju, M. Yarema, *Front Energy Res.* **2022**, *10*.
[25] F. Steinsiek, K. H. Weber, W. P. Foth, H. J. Foth, C. Schäfer *Wireless Power Transmission Experiment using an airship as relay system and a moveable rover as ground target for later planetary exploration missions*.
[26] Y. Komuro, S. Honda, K. Kurooka, R. Warigaya, F. Tanaka, S. Uchida, *Appl. Phys. Express* **2021**, *14*, 052002.
[27] K. Kurooka, T. Honda, Y. Komazawa, R. Warigaya, S. Uchida, *Applied Physics Express* **2022**, *15*, 052002.
[28] Y. L. Wong, S. Shibui, M. Koga, S. Hayashi, S. Uchida, *Energies* **2022**, *15*, 3690.
[29] Silvaco, *Silvaco software (version 5.0.10.R)*, https://silvaco.com/ (accessed: March 2020).
[30] N. Seoane, E. F. Fernández, F. Almonacid, A. García-Loureiro, *Prog. Photovoltaics* **2021**, *29*, 231.
[31] J. F. Lozano, N. Seoane, E. Comesaña, F. Almonacid, E. F. Fernández, A. García-Loureiro, *Solar RRL* **2022**, *6*.
[32] M. Ochoa, E. Barrigón, L. Barrutia, I. García, I. Rey-Stolle, C. Algora, *Prog. Photovoltaics* **2016**, *24*, 1332.
[33] M. Sotoodeh, A. H. Khalid, A. A. Rezazadeh, *J. Appl. Phys.* **2000**, *87*, 2890.
[34] A. S. Gudovskikh, N. A. Kaluzhniy, V. M. Lantratov, S. A. Mintairov, M. Z. Shvarts, V. M. Andreev, *Thin Solid Films* **2008**, *516*, 6739.
[35] K. J. Singh, S. K. Sarkar, in *Int. Conf. Energy Efficient Technologies for Sustainability*, **2016**, pp. 182–186.
[36] E. Ochoa-Martínez, L. Barrutia, M. Ochoa, E. Barrigón, I. García, I. Rey-Stolle, C. Algora, P. Basa, G. Kronome, M. Gabás, *Solar Energy Mater. Solar Cells* **2018**, *174*, 388.
[37] M. Levinshtein, S. Rumyantsev, M. Shur, *Handbook Series On Semiconductor Parameters*, World Scientific, **1996**.
[38] F. Ahmad, A. Lakhtakia, P. B. Monk, *Synth. Lect. Electromagn.* **2021**, *2*, 1.
[39] P. Huo, I. Lombardero, I. García, I. Rey-Stolle, *Prog. Photovoltaics* **2019**, *27*, 789.
[40] L. Barrutia, I. Garcia, E. Barrigon, M. Ochoa, I. Lombardero, M. Hinojosa, P. Cano, J. Bautista, L. Cifuentes, I. Rey-Stolle, C. Algora, *Spanish Conference on Electron Devices (CDE)* **2018**, 1.
[41] A. Luque, H. Steven. *Handbook of photovoltaic science and engineering*, Wiley, **2003**.
[42] P. Espinet González, *Advances in the modeling, characterization and reliability of concentrator multijunction solar cells*, **2012**.
[43] M. A. Green, *Solar cells: operating principles, technology, and system applications* **1982**, p. 274.
[44] J. F. Geisz, D. J. Friedman, M. A. Steiner, R. M. France, T. Song, *IEEE J. Photovolt.* **2023**, *13*, 808.
[45] N. A. Kalyuzhnyy, V. M. Emelyanov, V. V. Evstropov, S. A. Mintairov, M. A. Mintairov, M. V. Nahimovich, R. A. Salii, M. Z. Shvarts, *Thermal And Resistive Losses In InGaAs Metamorphic Laser ($\lambda = 1064$ Nm) Power Converters With Over 50% Efficiency*, **2019**, p. 050006.
[46] S. K. Reichmuth, H. Helmers, S. P. Philipps, M. Schachtner, G. Siefer, A. W. Bett, *Prog. Photovoltaics* **2017**, *25*, 67.
[47] G. Siefer, *Analyse des Leistungsverhaltens von Mehrfachsolarzellen unter realen Einsatzbedingungen* **2008**.
[48] T. Shan, X. Qi, *Infrared Phys. Technol.* **2015**, *71*, 144.
[49] C. Algora, V. Díaz, *Prog. Photovoltaics* **2000**, *8*, 211.
[50] J. F. Geisz, M. A. Steiner, I. García, S. R. Kurtz, D. J. Friedman, *Appl. Phys. Lett.* **2013**, *103*.
[51] S. Fafard, D. Masson, *Photonics* **2023**, *10*, 940.